Materialia 21 (2022) 101362

Contents lists available at ScienceDirect

Materialia

journal homepage: www.elsevier.com/locate/mtla

Energies and structures of Cu/Nb and Cu/W interfaces from density functional theory and semi-empirical calculations

R. Bodlos[a], V. Fotopoulos[b], J. Spitaler[a], A.L. Shluger[b], L. Romaner[a,c,*]

[a] Materials Center Leoben Forschung GmbH (MCL), Roseggerstraße 12, Leoben A-8700, Austria
[b] Department of Physics and Astronomy, University College London, Gower Street, London WC1E 6BT, UK
[c] Chair of Physical Metallurgy and Metallic Materials, Department of Materials Science, University of Leoben, Leoben, Austria

ARTICLE INFO

Keywords:
Interfaces
Adhesion
Density functional theory
Embedded atom method

ABSTRACT

Cu/Me multilayer systems, with Me referring to a body-centered cubic (*bcc*) metal, such as Nb and W, are widely used for nuclear, electrical, and electronic applications. Despite making up only a small percentage of the volume, interfaces in such systems play a major role in determining their electrical, mechanical, thermal and diffusive properties. Face-centered cubic (fcc) Cu often forms Kurdjumov-Sachs (KS) and Nishiyama-Wassermann (NW) type interfaces with *bcc* metals or variations thereof. For the Cu/Nb system, these interface relationships have been extensively studied with semi-empirical methods. Surprisingly, the energetics and interface properties of Cu/W have not yet been studied in detail, in spite of extensive applications. In this study, we employ both periodic Embedded Atom Method (EAM) and Density Functional Theory (DFT) simulations to explore the geometric and energetic properties of the KS and NW interfaces of Cu/Nb and Cu/W. To assess the reliability of our approach, the dependence of the results on the size of periodic cells is examined for coherent and incoherent interfaces. We provide the interface energies and the work of separation for the Cu/W and Cu/Nb interfaces at DFT accuracy. The results of calculations with two EAM potentials are in qualitative agreement with those obtained using DFT and allow investigating the convergence of interfacial properties. These key energetic quantities can be used for future thermodynamic and mechanical modeling of Cu/Me interfaces.

1. Introduction

Multilayer systems including interfaces between different metals are considered a novel family of materials with high potential for a broad range of applications. These include, for example, electronic devices as well as materials for aerospace and nuclear facilities where exceptional mechanical, electrical and thermal properties in high strain conditions and high-temperature thermal cycling conditions are necessary [1–5]. However, the properties of multilayer systems often deviate significantly from the properties of their respective bulk counterparts, with the origins of these deviations yet not fully understood [6]. Some of the major factors that determine these properties are film deposition methods, film morphology and thickness. For example, the thickness of deposited layers plays an important role for the mechanical stability of Cu/Nb and for general *fcc/bcc* interfaces [7]. Thus, adjusting the layer thickness can result in materials with different properties. The effect of thickness has been investigated for several metallic interfaces, including Al/Nb, Zr/Nb, Cu/Nb, and Cu/W [7].

Interfaces play an even more important role in nanoscale multilayer systems [6] where the interface occupies a significant fraction of the total volume, especially when compared to bulk materials. Important characteristics, such as interface energy (γ) and work of separation (WoS), strongly affect their mechanical and thermodynamic properties [8,9]. Additionally, interfaces serve as sources and sinks for defects, affecting the multilayers' resilience against degradation occurring during plastic deformation [7]. Also, improved properties at the nano scale have been reported to correlate with interfacial defect formation mechanisms, which are still not fully understood [10].

In general, *fcc/bcc* multilayer systems often form interfaces obeying either the Kurdjumov-Sachs (KS) or the Nishiyama-Wassermann (NW) orientation relationship [1,11–13]. In this work,we focus on modeling KS and NW interfaces of Cu with Nb or W. Analysis of Cu/Nb and Cu/W multilayers using X-Ray diffraction and electron microscopy suggest the presence of either KS or NW or both interface types [2,14,15]. Furthermore, multilayers that were created using severe plastic deformation such as accumulative roll bonding have been observed to form interface types that, while following the KS or NW orientation relationship, show different interface planes and different mechanical properties [1,11]. The Cu/W and Cu/Nb systems are both not miscible in the solid phase [2,16,17]. Due to the considerable lattice mismatch between Cu and W (15%) or Nb (10%) the interface is incoherent [18–21].

* Corresponding author.
E-mail address: lorenz.romaner@unileoben.ac.at (L. Romaner).

https://doi.org/10.1016/j.mtla.2022.101362
Received 31 January 2022; Accepted 10 February 2022
Available online 13 February 2022

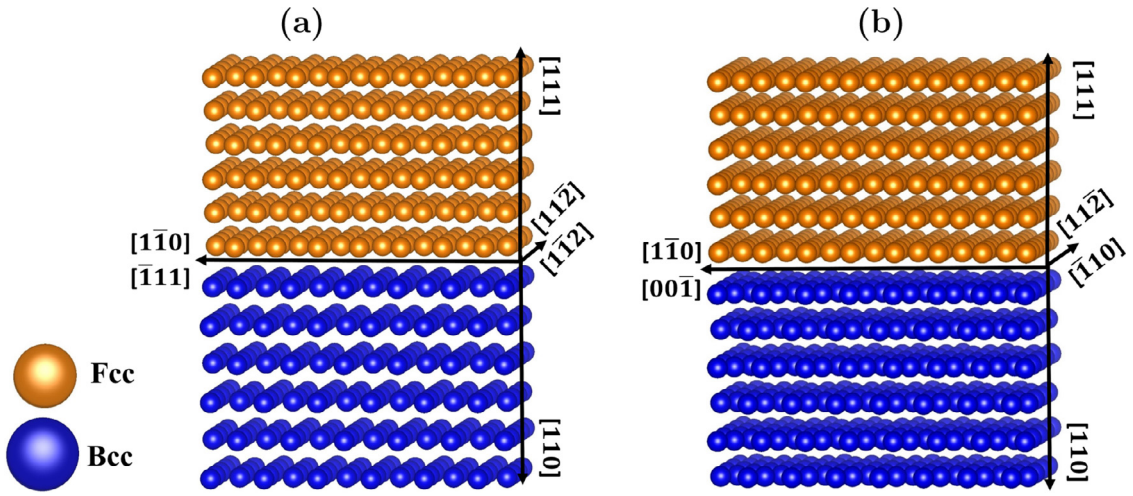

Fig. 1. The examined interface orientational relationships: (a) Kurdjumov-Sachs and (b) Nishiyama-Wassermann models. The two orientations differ by a rotational angle of 5.26°. Both NW and KS include the closest packed surfaces of the two crystals, namely in the case of an *fcc* and a *bcc* lattice these are the (111) and (110) surfaces, respectively.

Both molecular dynamics (MD) and density functional theory (DFT) simulations have revealed important properties of Cu/Nb and Cu/W interfaces. For example, MD simulations of Cu/Nb demonstrated that interfaces under mechanical load give rise to the formation of dislocations and initiation of Shockley partial dislocation loops [1,22,23]. Investigations of the misfit dislocation network of the NW and KS Cu/Nb system via the atomically informed Frank-Bilby theory have been carried out [24]. The γ values of Cu/Nb KS and NW interfaces have been predicted using the embedded atom method (EAM) to amount to 0.54-0.57 J/m^2 [25,26] and 0.59 J/m^2 [26], respectively. DFT calculations of coherent cells of Cu/W NW interfaces [27,28] predicted γ values in the 0.78-1.14 J/m^2 range. In general, DFT and MD interface simulations almost invariably employ periodic boundary conditions [14,25,29].

In order to accurately simulate interface energetics, interface geometry or dislocation phenomena, large-scale models of thousands of atoms are required. Such simulations are only feasible with interatomic potentials using methods such as EAM [30–32]. Often such potentials are optimized for basic properties, such as surface energies, elastic constants or vacancy formation energy in a given crystal structure and their performance for more complex defects, such as dislocations and interfaces between different crystals, is unclear. Testing the accuracy of these potentials for modeling interface properties requires detailed comparison with the results of more accurate DFT calculations. However, periodic DFT methods can only treat systems of up to 1000 atoms, which may not be large enough to fully describe interface properties of two metals [30–32]. It is often unclear which approximation introduces a larger error, the interatomic potential or the small cell size.

In this work, we provide a systematic comparison between EAM and DFT for KS and NW interfaces of Cu/Nb and Cu/W. We focus on calculating γ and WoS and their convergence with the periodic cell size and closely analyse the geometry of the interface. A large interface always accommodates a misfit dislocation network, as shown in previous works [24]. A fully converged misfit dislocation network that allows both Cu and W to be within their native lattice parameters is only accessible via EAM. However, smaller cells below 300 atoms also include misfit dislocations where the strain is already greatly reduced compared to the smallest possible cell, which corresponds to the fully coherent cell. Although this coherent cell can be regarded as unrealistic in experiments, it provides insights into the nature of the Cu/Me bond at the interface. Indeed, many investigations have targeted the description of large cells based on the gamma surface of the coherent interface combined with continuum modeling based on the Peierls-Nabarro approach [29,33–40]. In this work we do not use such an approach to quantitatively describe γ values. Rather, we use the gamma surface of the coherent cell to qualitatively understand the structural relaxation inside incoherent interfaces. Our route to reliable interface energetic is to model small interfaces with DFT directly and use EAM to assess the convergence of the obtained values.

2. Methodology

2.1. Orientation relationships

The KS and NW orientation relationships are defined by the directions parallel to each other, namely Cu[1$\bar{1}$0]//W[$\bar{1}$11], Cu[11$\bar{2}$]//W[1$\bar{1}$2] and Cu[111]//W[110] for KS, and Cu[1$\bar{1}$0]//W[00$\bar{1}$], Cu[11$\bar{2}$]//W[$\bar{1}$10] and Cu[111]//W[110] for NW. Both the NW and KS interface models include the closest packed surfaces of the two crystals as the interface planes, that in the case of an *fcc* and a *bcc* lattice are the (111) and (110) surfaces, respectively (Fig. 1). Those two orientation relationships differ by a rotational angle of 5.26° and can therefore be transformed into each other [11–13]. Note that other variants of NW and KS interfaces were also discussed in literature where they were denoted as ARB-LR and ARB-CR interfaces, respectively, as they occur in accumulative roll bonding experiments [1,11]. While these interfaces also fulfill the NW and KS orientation relationship, respectively, they have different interface planes, Cu(112) and Me(112) for ARB-LR, and Cu(111) and Me(110) for ARB-CR. We do not consider these interfaces here, since they only occur in special circumstances.

2.2. DFT Calculations

To carry out DFT calculations, the Vienna Ab-Initio Simulation Package (VASP) [41,42] was used with the Perdew-Burke-Ernzerhof (PBE) exchange-correlation functional [43,44]. For the systems considered here, PBE has been shown to be more accurate compared to other meta-GGA and GGA functionals, though it has also been reported to underestimate both the work function and surface energies for some of the metals [45,46]. No dispersion correction has been included as van der Waals interactions are considered to be negligible in the case of metal-metal interfaces [46,47]. Figure 1 shows the surface orientations examined for this study. All the structures are shown prior to geometry optimization. For all the simulations, the individual pure metallic systems have not been relaxed before the relaxation of the multilayer system. The k-point mesh was chosen to fulfill the criterion that k-point mesh times

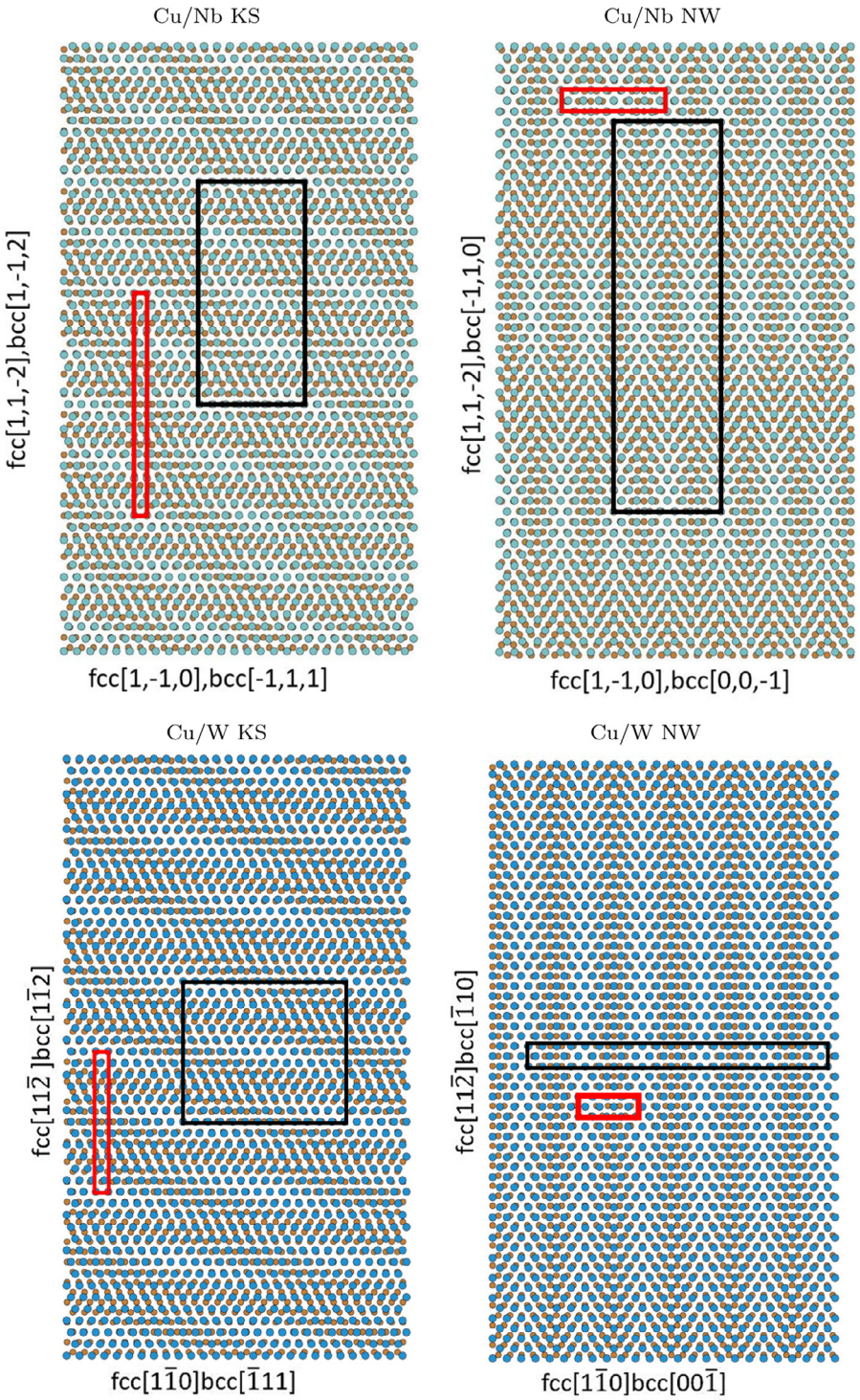

Fig. 2. Optimal Cu/Nb and Cu/W interface cell sizes in both of the examined orientations (KS and NW) for the EAM (Black) and DFT (Red) cells. (For a coloured version of the figure, the reader is referred to the web version of this article.)

cell length (in Å) lies between 30 and 40 for each direction. A cut-off energy of 300 eV was used. For geometry optimization the conjugated gradient algorithm was used. Copper was treated using 11 valence electrons ($3d^{10}4s^1$), W using 12 valence electrons ($5p^6 5d^4 6s^2$) and Nb using 11 valence electrons ($4p^6 4d^4 5s^1$), respectively.

2.3. EAM Calculations

The simulations using forcefields were performed using the Large-scale Atomic/Molecular Massively Parallel Simulator (LAMMPS) code as implemented in the ASE python module [22,48]. The Broyden-Fletcher-Goldfarb-Shanno (BFGS) minimization algorithm was used for geometry optimization [49].

For the Cu/W system, the potential developed by Zhou et al. [50] was used. The potential was fitted to lattice parameters, cohesive energies and elastic constants for the individual metals. The potential was obtained via the Interatomic Potentials Repository and OpenKIM [51,52]. For Cu/Nb the potential developed by Demkowicz and Hoagland [10] was used. This potential has been developed through analytic fitting of the phase diagram of Cu/Nb along with other properties, such as bulk modulus and lattice parameters [50,51] and has in total seven adjustable parameters [53].

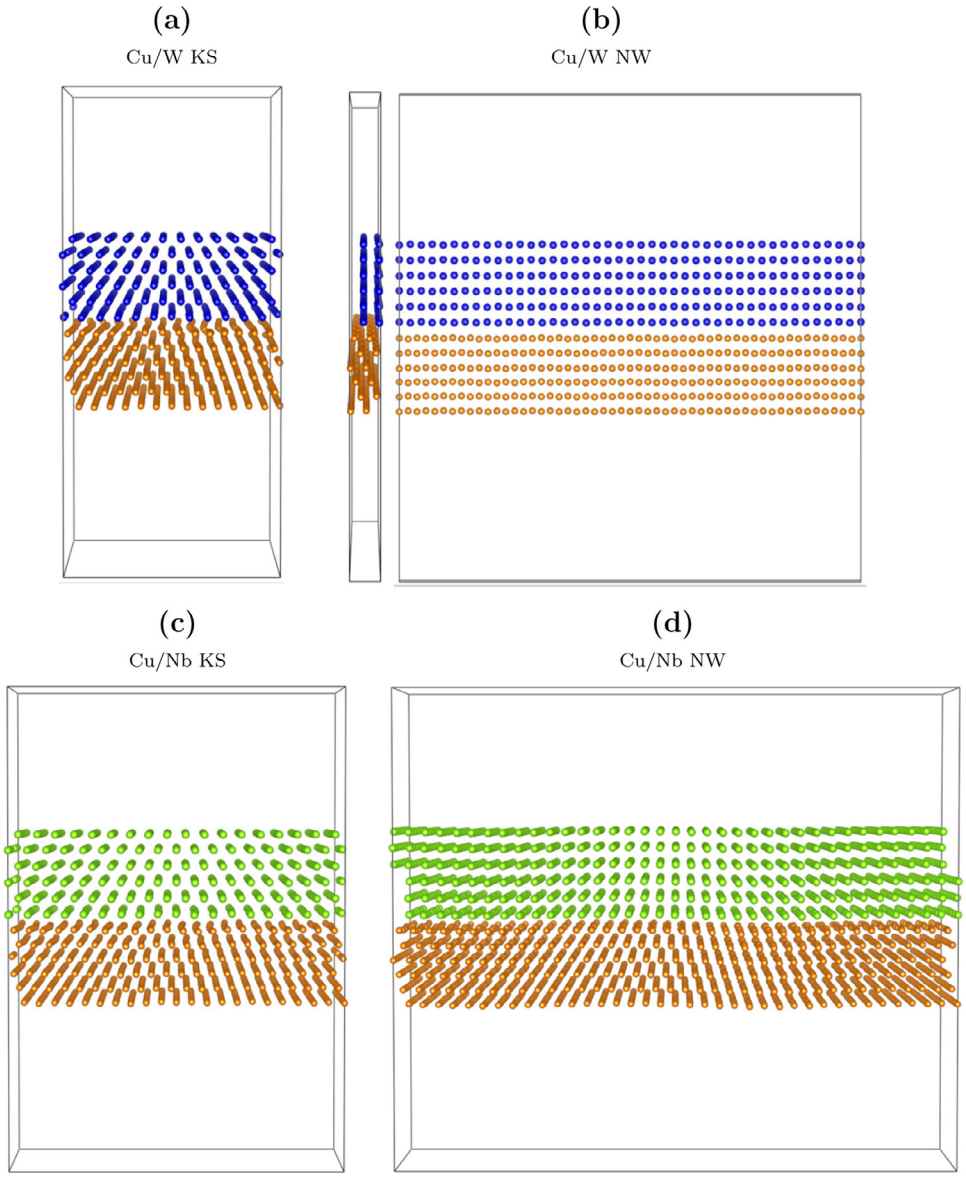

Fig. 3. (a)Cu/W KS, (b) Cu/W NW, (c) Cu/Nb KS (d) Cu/Nb NW Cell after relaxation. Cu, W and Nb atoms are shown in orange, blue and green colours, respectively.(b) is shown from 2 sides as it is considerably longer in one direction. When comparing Cu/W with Cu/Nb both potentials show the same relaxation effects close to the interface region. (For a coloured version of the figure, the reader is referred to the web version of this article.)

The python module ASE was used for constructing the defect geometries with multiple options readily available within the code for manipulation of atoms [48]. For the visualisation of the resulting configurations VESTA - JP-Minerals and ASE's GUI were used [48,54].

2.4. Simulation cell and stress balancing method

Simulation cells for the Cu/Me interface, were Me is W or Nb, are constructed by combining a slab of Cu and a slab of Me into one common cell. The building block for the slabs are rectangular. For Cu it has the following dimensions in x and y direction, $l_{Cu(x)} = |u_{[110]}|$, $l_{Cu(y)} = |u_{[112]}|$ where u denotes vectors connecting two neighboring atoms along the specified crystallographic direction in the Cu lattice. Equivalently, the dimensions are $l_{Me(x)} = |u_{[111]}|$ and $l_{Me(y)} = |u_{[112]}|$ for KS and $l_{Me(x)} = |u_{[001]}|$ and $l_{Me(y)} = |u_{[110]}|$ for NW in the bcc lattice. These building blocks are repeated $n_{Cu(x,y)}$ and $n_{Me(x,y)}$ times to create the Cu and Me slab, respectively. We use the notation (x, y) to indicate that the expression can be used for x or y. If the native Cu and Me lattice parameters are used, a residual difference

$$\Delta_{(x,y)} = |n_{Cu(x,y)} l_{Cu(x,y)} - n_{Me(x,y)} l_{Me(x,y)}| \tag{1}$$

arises, which has to be removed when accommodating the slabs in a common periodic cell. For this purpose we use the stress-balancing method, which is based on continuum linear elastic theory [55]. The values of elastic constants can be found in the Appendix, Table 5. The strain introduced in the slabs with the stress balancing model is quantified by the misfit M defined as:

$$M_{(x,y)} = \frac{\Delta_{(x,y)}}{l_{Me(x,y)} * n_{Me(x,y)}} \tag{2}$$

In the z direction, the cell size is such that the W and Cu slabs can be accommodated together with a vacuum gap of 10 Å to decouple periodic images. The units of repetition along the z direction were 2 and 3 unit cells for Me and Cu, respectively, to ensure that the thickness of the two slabs is comparable.

2.5. Gamma surface approach

To calculate the gamma surface of the coherent interface, the Cu slab is displaced rigidly with respect to the Me slab and the geometry optimization is carried out in z direction while keeping x and y positions of the atoms fixed.

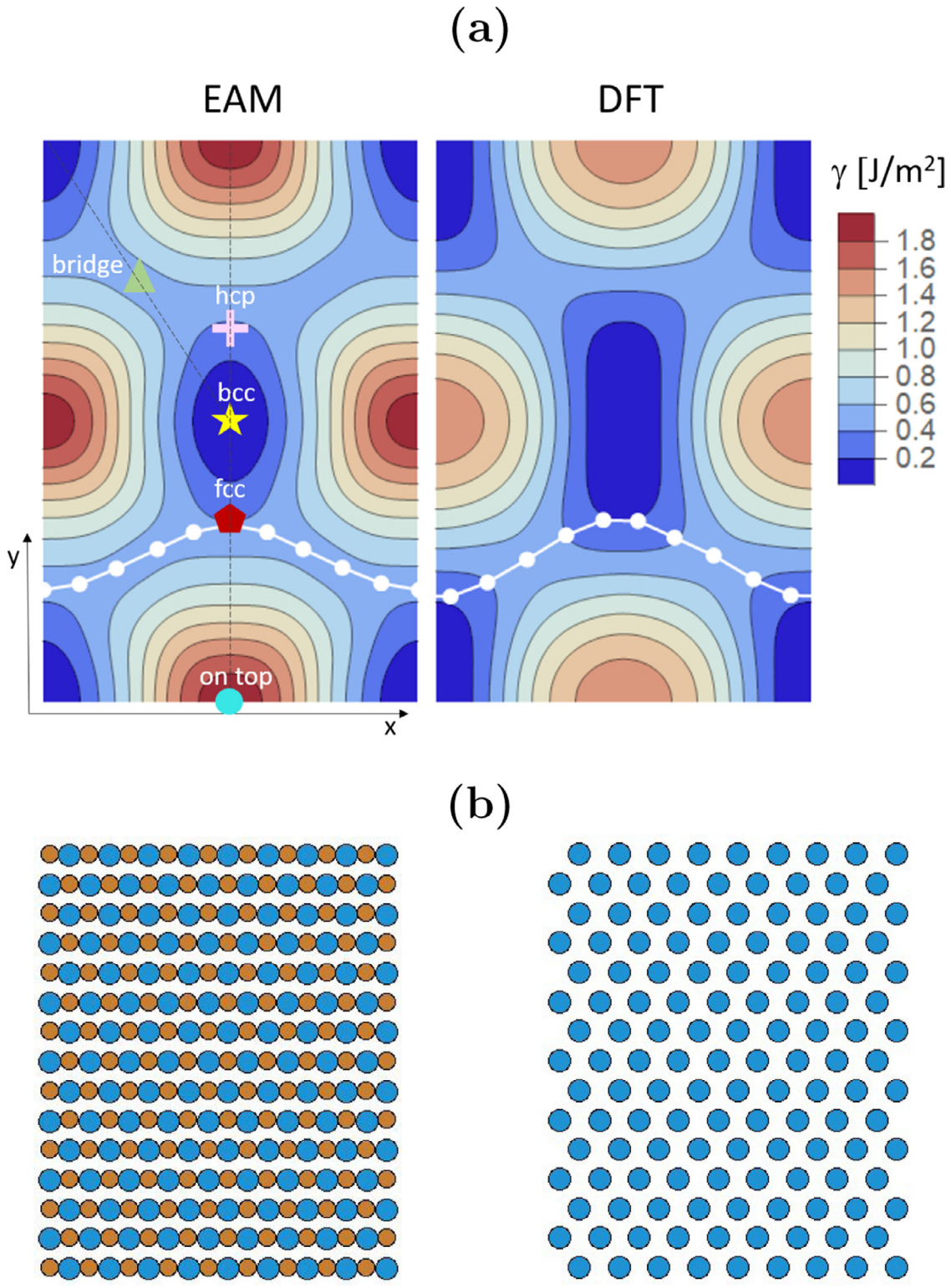

Fig. 4. (a) NW gamma surface of EAM and DFT calculations for the Cu/W interface represented as a contour plot. Special points corresponding to bcc, fcc, hcp stacking, the bridge position and the on top position are highlighted with symbols. The points resulting from structural relaxation of the small incoherent NW interface are shown in white. (b) Structure at the lowest(left) and highest(right) energy of the gamma surface corresponding to bcc and on top stacking, respectively. In the right plot Cu atoms are not visible as they are aligned exactly on top with the W atoms. (For a coloured version of the figure, the reader is referred to the web version of this article.)

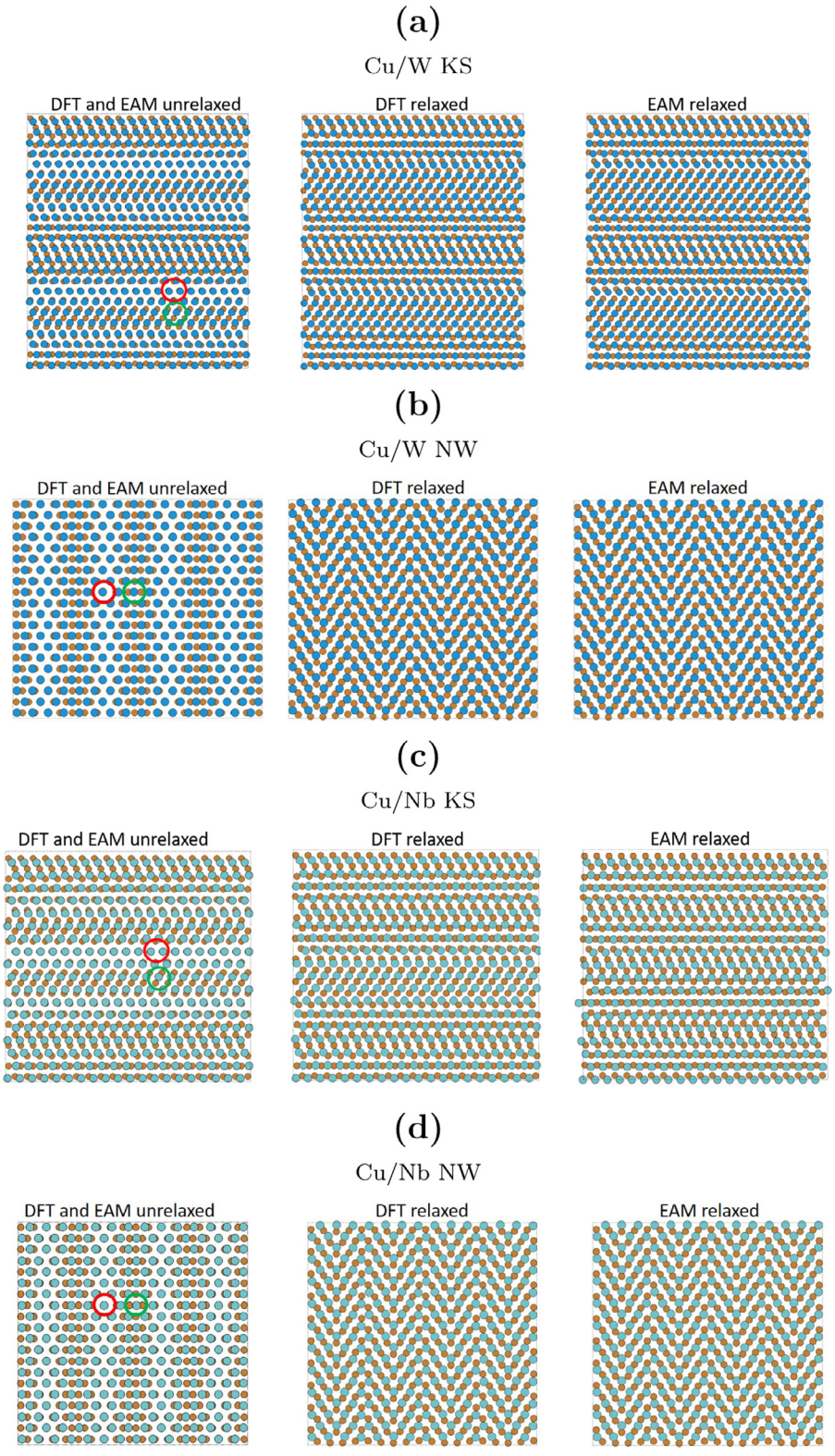

Fig. 5. Small incoherent supercell for (a) Cu/W KS DFT and EAM before and after relaxation (b) Cu/W NW DFT and EAM before and after relaxation (c) Cu/Nb KS DFT and EAM before and after relaxation (d) Cu/Nb NW DFT and EAM before and after relaxation. The red and green circles show areas of maximum and minimum energy respectively. (For a coloured version of the figure, the reader is referred to the web version of this article.)

A modification of the gamma surface approach following Ref [56] is also used to find the optimal interface structure of incoherent supercells. Using this approach, the two slabs are shifted in x and y directions with respect to each other using a predefined spacing step and all atoms are relaxed along x, y, z coordinates. From all the so obtained relaxed structures, the one corresponding to the energy minimum is selected.

2.6. Interface simulation

The properties of interfaces with KS and NW orientation relationship were calculated using periodic boundary conditions. The surface energies for the pure metallic systems were calculated using the following

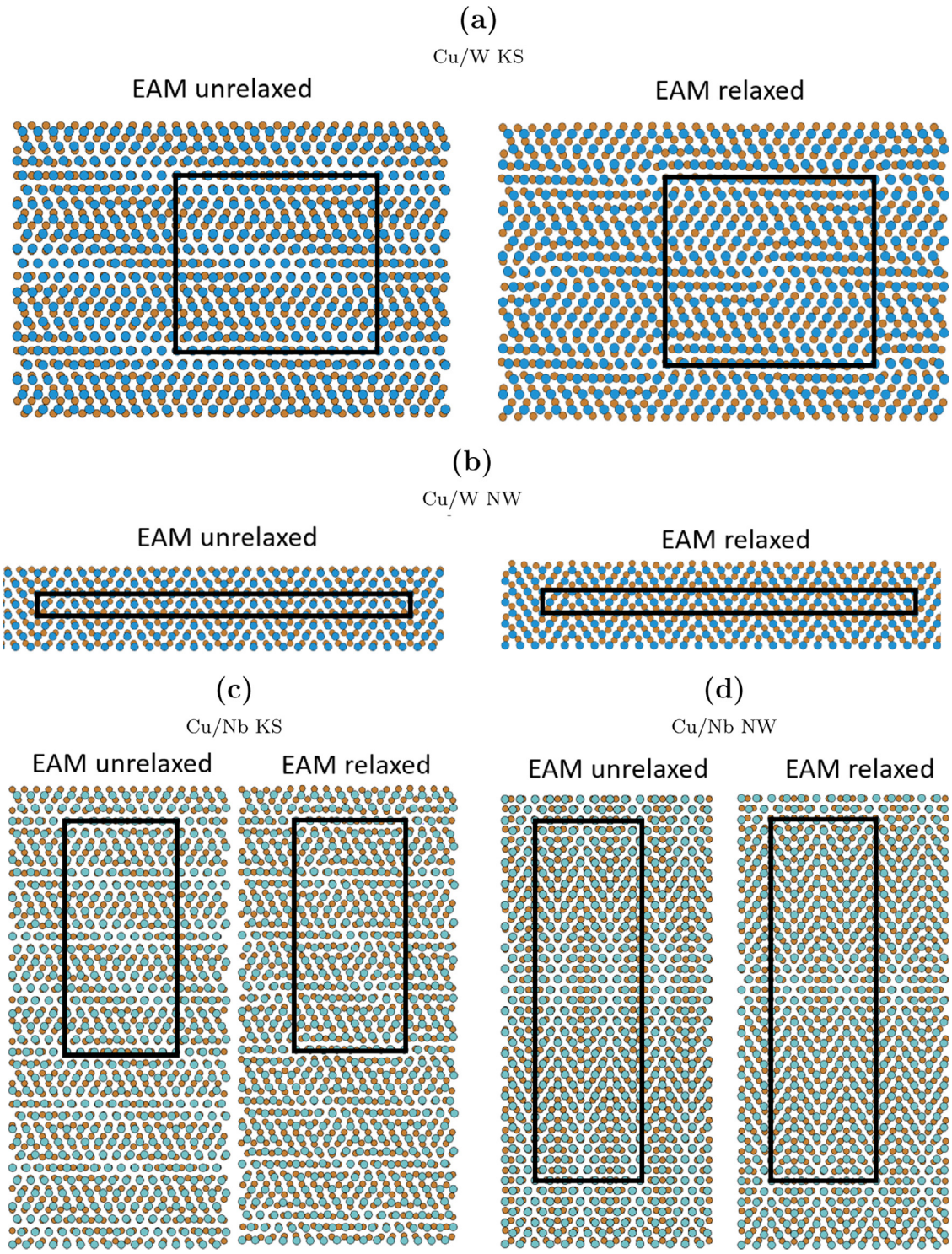

Fig. 6. Large incoherent supercell for (a) Cu/W KS EAM before and after relaxation (b) Cu/W NW EAM before and after relaxation (c) Cu/Nb KS EAM before and after relaxation (d) Cu/Nb NW EAM before and after relaxation.

relation:

$$\gamma_S = \frac{E_{(Cu,W,Nb)} - (N * E_{B_{(Cu,W,Nb)}})}{2A}. \quad (3)$$

where $E_{Cu,W,Nb}$ are the energies of the individual Cu,W and Nb lattices with free surfaces, N the number of Cu, W or Nb atoms and $E_{B_{(Cu,W,Nb)}}$ the energy per atom in bulk *Cu, W* and *Nb*, respectively. A is the surface/interface area.

In order to calculate the WoS, which corresponds to the energy needed to completely dissociate the bonds at the interface, the following relation was used:

$$W_{sep} = \frac{E_{Cu} + E_{Me} - E_{Cu/Me}}{A}. \quad (4)$$

Here E_{Cu} and E_{Me} are the energies of the Cu and Me slab while $E_{Cu/Me}$ is the energy of the Cu/Me interface. The size of the unit cell along x,y,z is the same for $E_{Cu/Me}$, E_{Cu} and E_{Me}.

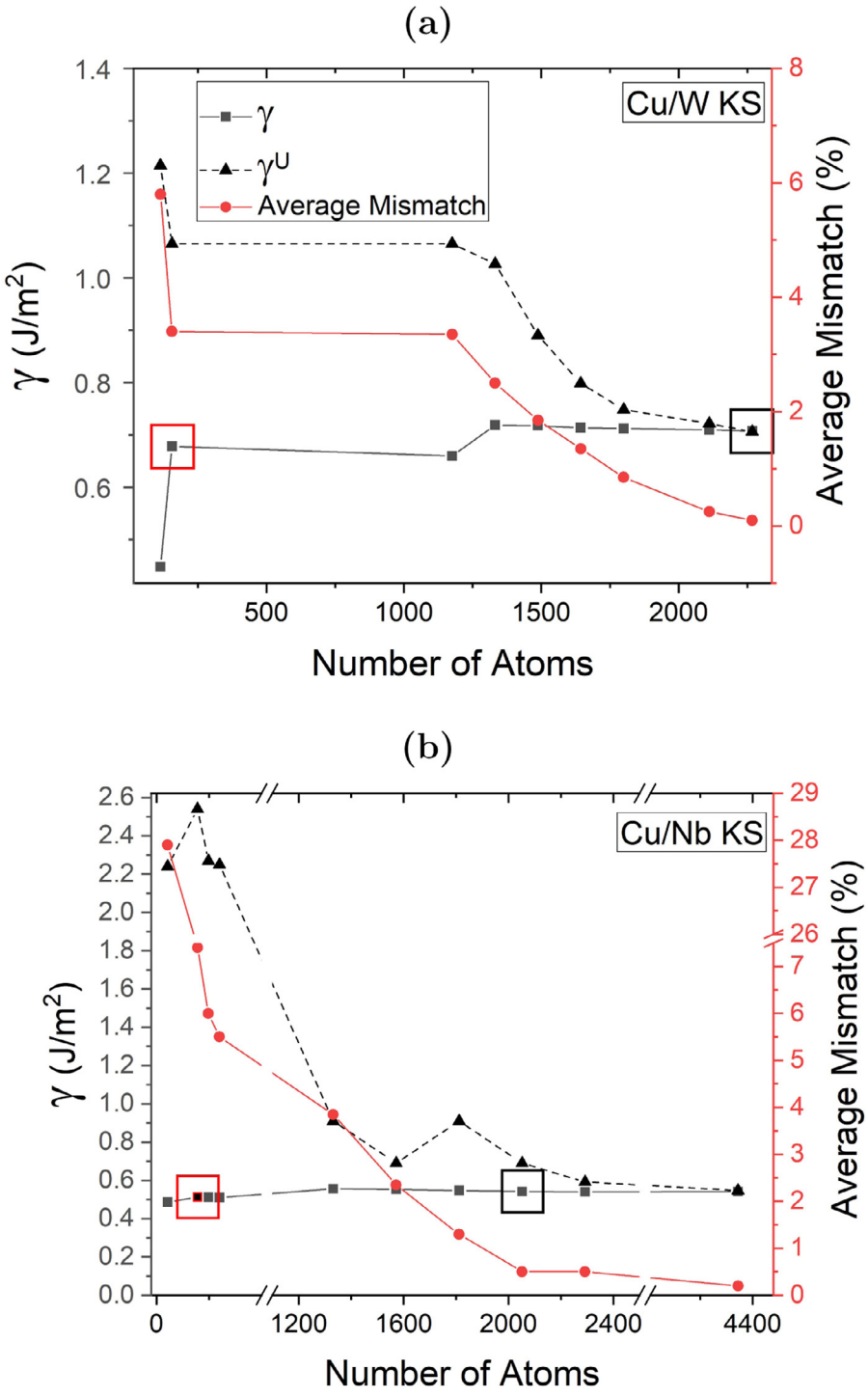

Fig. 7. (a) Cu/W and (b) Cu/Nb γ values (γ) size convergence for the KS interface. The unstrained values, γ^U, along with the average mismatch in x and y directions are also included. The red and black squares correspond to the small and large interface cells discussed in Section 3.2 and shown in Fig. 2. (For a coloured version of the figure, the reader is referred to the web version of this article.)

To calculate γ, the energy cost to introduce an interface into the two bulk materials is calculated as:

$$\gamma = \frac{E_{Cu/Me} - \frac{E'_{Cu}+E'_{Me}}{2}}{A}. \quad (5)$$

In this case, E'_{Cu} and E'_{Me} are the energies of the Cu and Me slabs, respectively, while doubling the number of layers compared to the supercell used for calculating E_{Cu} and E_{Me} shown in Eq. (4). Again, the size of the unit cell is the same for $E_{Cu/Me}$, E'_{Cu} and E'_{Me}.

Finally, to determine the effect that strain has on the Cu/W and Cu/Nb energetics, a second relation was used for calculation of γ. In this case the interface energy also contains the strain energy which is needed to accommodate the Cu and Me slabs in a common unit cell. This energy is referred to as unstrained interface energy γ^U which is defined as:

$$\gamma^U = \frac{E_{Cu/Me}}{A_{Cu/Me}} - \frac{\frac{E'^U_{Cu}}{A_{Cu}} + \frac{E'^U_{Me}}{A_{Me}}}{2}. \quad (6)$$

For the calculation of E'^U_{Cu} and E'^U_{Me}, the cell dimensions along x and y were chosen according to the lattice constants of pure Cu and Me. Therefore the areas of each cell involved (A_{Cu} and A_{Me}) are no longer identical to the ones of the interface cell ($A_{Cu/Me}$). Note that the defini-

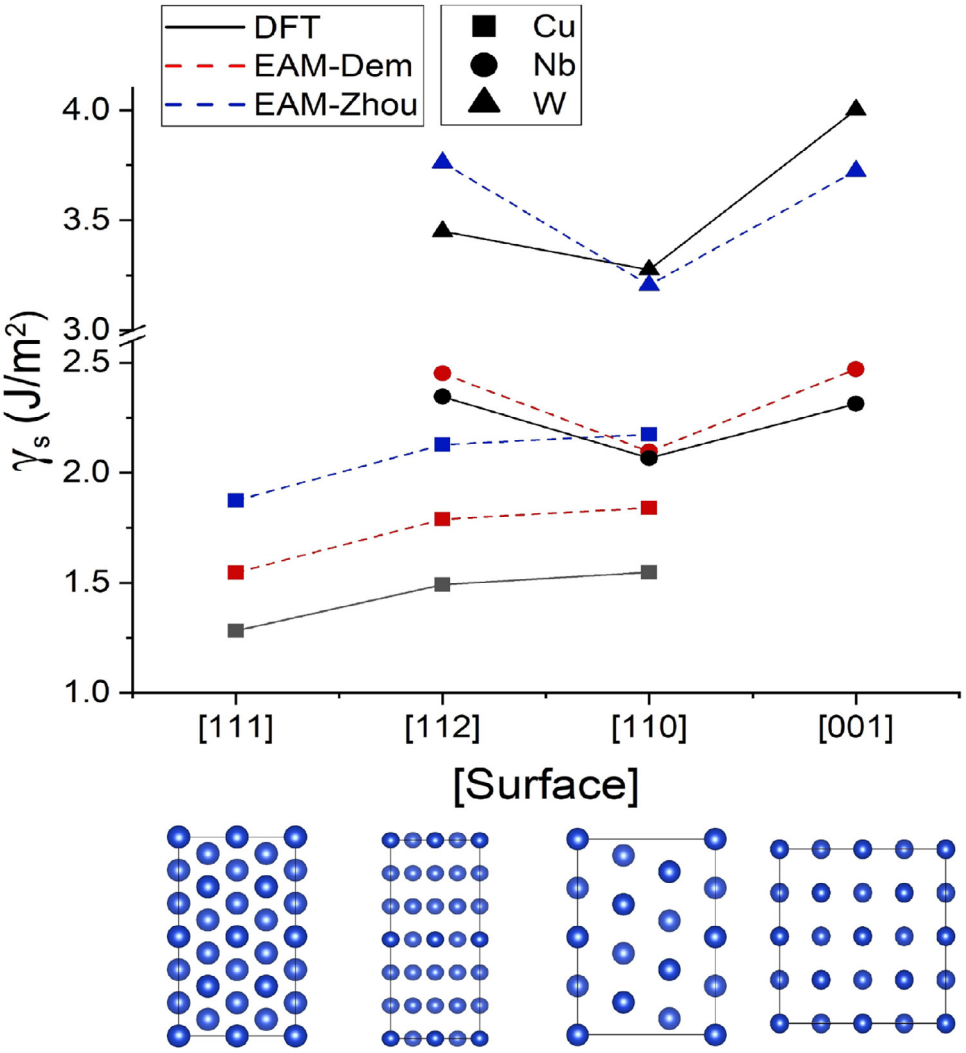

Fig. 8. Surface energy for pure Cu, W and Nb as obtained from DFT and EAM. Bottom images illustrate the top views of the 4 examined surfaces for copper prior to relaxation. Distinctive differences compared to DFT were reported in the case of the examined surfaces for W and Cu using the potential developed by Zhou et al. [50] The potential developed by Demkowicz et al. [10] was found to accurately match the DFT γ_S for all the examined surfaces.

Table 1
Dimension of unit cells of Cu and Me along x and y direction, $l_{Cu(x,y)}$ (Å), $l_{Me(x,y)}$ (Å), ratio $R_{(x,y)}$ and sequence of best rational approximations $n_{Me(x,y)}/n_{Cu(x,y)}$ for the KS and NW interface. The star and cross indicates the unit cell size corresponding to the black and red rectangle in Fig. 2, respectively.

System	$l_{Cu(x)}$	$l_{Me(x)}$	R_x	$n_{Me(x)}/n_{Cu(x)}$ sequence
KS, Nb	2.556	2.859	0.894	$1/1^{+}$ 8/9* 17/19 59/66
NW, Nb	2.556	3.301	0.774	1/1 3/4 7/9^{*+} 24/31 199/257
KS, W	2.556	2.741	0.933	$1/1^{+}$ 13/14 14/15* 69/74 152/163
NW, W	2.556	3.165	0.808	1/1 4/5^{+} 21/26* 277/343
	$l_{Cu(y)}$	$l_{Me(y)}$	R_y	$n_{Me(y)}/n_{Cu(y)}$ sequence
KS, Nb	4.427	8.086	0.547	1/1 1/2 5/9 6/11^{*+} 23/42 98/179
NW, Nb	4.427	4.668	0.948	$1/1^{+}$ 18/19* 37/39 55/58 147/155 349/368
KS, W	4.427	7.753	0.571	1/1 1/2 4/7^{*+} 189/331 193/338
NW, W	4.427	4.476	0.989	$1/1^{*+}$ 90/91 181/183 271/274

tions of unstrained and strained γ values as well as WoS are analogous to previous works, see e.g. [29,40,57].

3. Result of calculations

3.1. Cell size

As computational resources are limited, simulation cells have to be limited to a size that fulfills both the need for accurate, representative results and can be calculated with reasonable computational effort. To determine the optimal cell size for the interface, the unit cell lengths in the x and y direction of Cu and Me need to match as closely as possible. The sequence of optimal units of repetition emerge by truncating the continued fraction expression of the ratio

$$R_{x,y} = \frac{l_{Cu(x,y)}}{l_{Me(x,y)}} = \frac{1}{a_1 + \frac{1}{a_2 + \frac{1}{a_3 + \ldots}}} \tag{7}$$

at increasingly higher coefficients a_n which can be determined via a standard algorithm. This truncated ratio can be represented by a simple

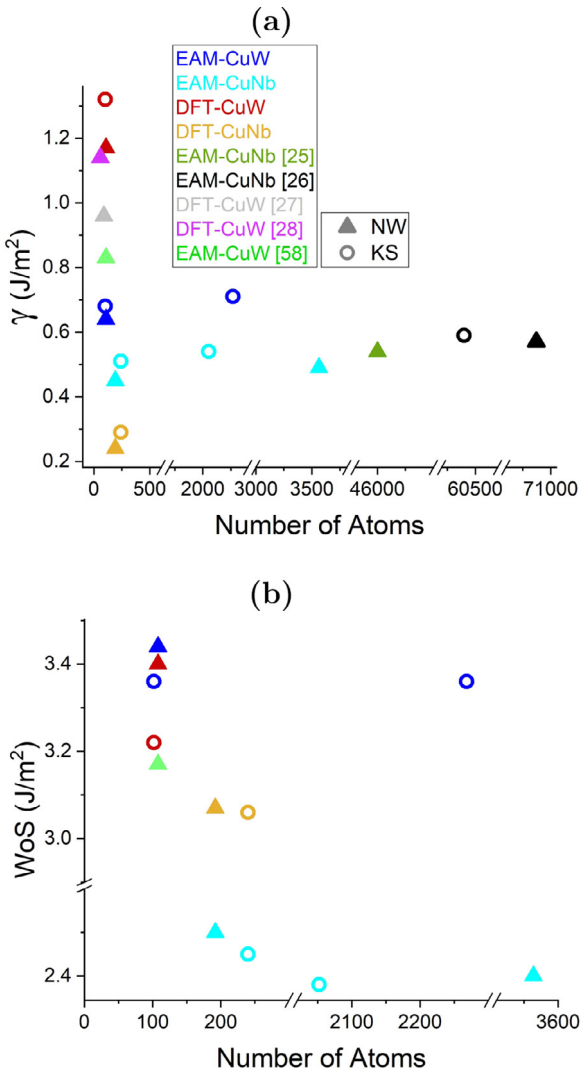

Fig. 9. γ and WoS comparison between EAM and DFT. The reported literature values for the γ are also included [25–28,58]. The potential developed by Demkowicz et al. [10] used for our Cu/Nb calculations showed an offset of approximately 0.2 J/m^2 for γ and 0.5 J/m^2 for the WOS compared to DFT. The potential developed by Zhou et al. [50] used for our Cu/W calculations showed singnificantly lower γ values compared to DFT, however the WOS match the DFT results closely. (For interpretation of the references to colour in this figure legend, the reader is referred to the web version of this article.) Data are provided also in Table 4 in the Appendix.

fraction of two integer numbers, $n_{Cu(x,y)}/n_{Me(x,y)}$. The obtained sequence allows to minimize $\Delta_{(x,y)}$ for cells of increasing number of atoms.

The sequence of best rational numbers so obtained is shown in Table 1. To select the small or large incoherent supercells discussed in Section 3.2, where the former is treated with DFT and EAM while the latter only with EAM, the limits of the largest cell was set to 3600 atoms for the large incoherent supercells and 250 for the small incoherent supercells. This corresponds to the rational number identified by the star or cross in the table for EAM and DFT, respectively. These choices correspond to the black and red cells in Fig. 2. Overall, the number of atoms in the simulation cells range from 102 atoms for the red Cu/W KS cell to 3564 atoms for the black NW Cu/Nb cell. The red cells will be denoted as small incoherent cells while the black cells will be denoted as large incoherent cells in the following.

Fig.3 shows the obtained largest cells optimized with EAM for each system. In general, the slabs remain flat and most of the rearrangements take place directly at the interface. To reveal the structural relaxation taking place at the interface, we will now investigate more systematically cells of increasing size and focus on the two layers immediately adjacent to the interface.

3.2. Interface structure

3.2.1. Coherent cells

The coherent cell represents the starting point of our analysis since it defines the Burgers vector of the misfit dislocation network of the large inchorerent supercells. Furthermore, the associated gamma surface allows to interpret the geometry and energetics of the relaxed interface with concepts analogous to the Peierls-Nabarro approach for a dislocation in bulk [29,33–40].

For the coherent cell, $n_{Me(x,y)}/n_{Cu(x,y)} = 1/1$ and the mismatch $M_{x,y}$ corresponds to $R_{x,y}$. From Table 1 it can be seen that $R_{x,y}$ deviates considerably from 1 in the NW case (by about 25%) and strongly in the KS case along the y direction (by about 100%). For the latter $n_{Me(y)}/n_{Cu(y)} = 1/2$ would be a more reasonable assumption for the definition of the coherent cell. However, with this definition a misfit dislocation in the fcc lattice would have a [112] Burgers vector, which according to Frank's rule would readily dissociate into two smaller Burgers vectors of 1/2[112]. Therefore the value of such a gamma surface would be limited. It is more appropriate to interpret the large incoherent supercells of the KS orientation also with the coherent NW cell since the two only differ by a rotation of 5.26°.

As can be seen in Fig. 4, the Cu/W gamma surface shows a relatively straightforward shape with a maximum when the W and Cu atoms are aligned exactly on top of each other, and a minimum when they are displaced by a half period along the x directions. Note that these positions have been termed the bcc stacking site and the on-top site, respectively [57]. The bridge, fcc and hcp sites exhibit intermediate energies. The reference energy in the plot is the bcc stacking site for which the absolute value of γ is 0.99 J/m^2 using DFT. The general shape of the gamma surface is similar in both EAM and DFT with the difference that the maximum is higher for the former. For the Cu/Nb system, the shape of the gamma surfaces with DFT and EAM are analogous and not reported here. Further tests were also carried out for cells with other lateral dimensions as obtained from the stress balancing model. These comprise the two limiting cases where the lateral dimension correspond to the one of Cu or W as well as their simple average. The results along the diagonal direction are shown in the Appendix (see Fig. 10), where it emerges that considerable variations arise. However, only the height of the peak is affected but not the general shape of the gamma surface.

Note that other works have also reported on the NW coherent gamma surface. Ref. [58] has investigated the gamma surface of Cu/W to address the theoretical shear strength employing the same EAM potential as the one used here. The gamma surface matches that of this work, however, as the main focus of the paper was the buckling of Cu/W layers, the analysis of the gamma surface and misfit dislocation was focused on elasticity and not on interface structure. Other works have focused on different fcc/bcc combinations including Cu/Ta [57] or Ag/Fe [29]. In these works, also the bcc stacking was the most favorable and the on top stacking the least favorable. The relative alignment of bridge and fcc stacking was the same for Cu/Ta but not for Ag/Fe. We note here that for Cu/Nb no gamma surfaces have been published despite the considerable attention that the system has been received in research on misfit dislocations.

3.2.2. Small incoherent interface cells

When the ratio of repetitions $n_{Me(x,y)}/n_{Cu(x,y)}$ differs from 1/1, a misfit dislocation network is introduced in the cell. Every choice of the sequence of rational numbers of Table 1 would lower the elastic strain in the slabs compared to the coherent cell, where the strain release is higher the larger the denominator. We first focus on the red cells and later on the black cells in Fig. 2. In accordance with previous work [29], we could call the red cells "semi-coherent", since they are still coherent

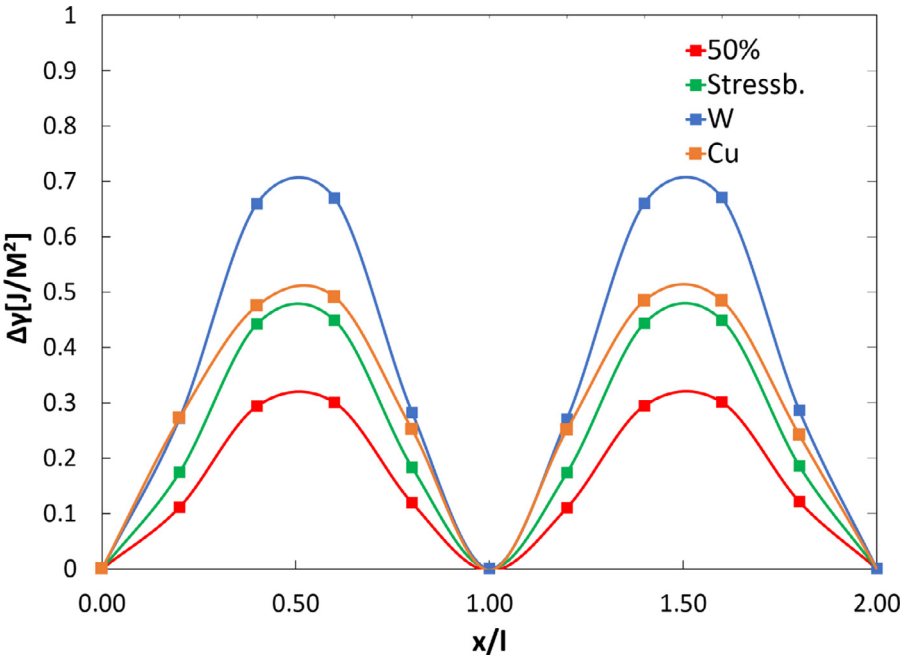

Fig. 10. Influence of different lattice parameters on the gamma surface when the lattice parameter is constrained to the one of W (3.185Å, blue), Cu (2.571Å, orange), the result of the stress balancing model (2.984Å, green) and the arithmetic average of Cu and W (2.878Å, red). (For interpretation of the references to colour in this figure legend, the reader is referred to the web version of this article.)

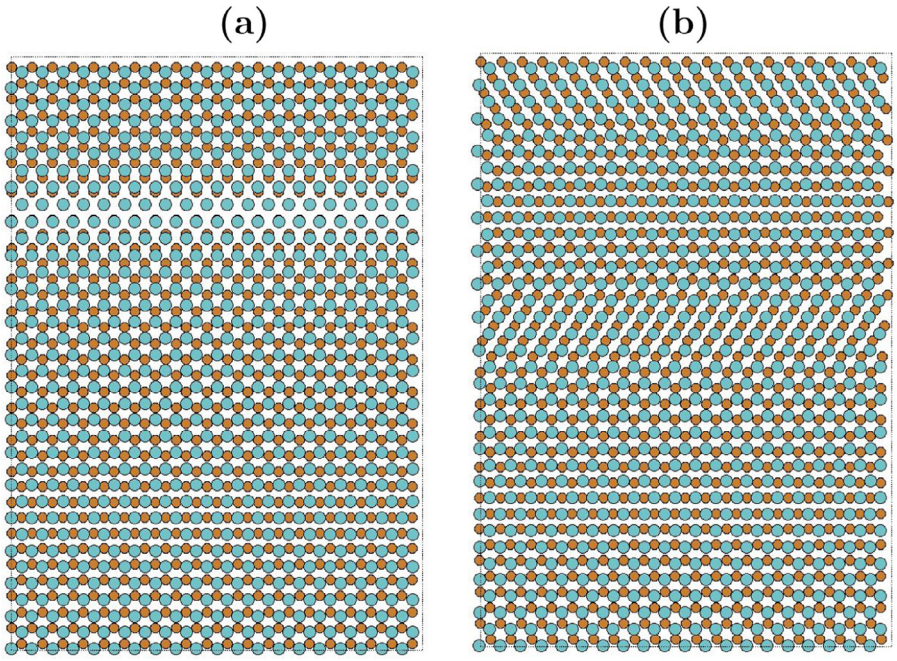

Fig. 11. Cu/Nb small incoherent supercells with (a) single dislocation and (b) split of dislocation into two dislocations after relaxation.

in 1 dimension and call the black cells ”incoherent” since they have misfit dislocations introduced in 2 dimensions. However the term ’semi-coherent’ is also used differently, see e.g. [14,59]. In these works, ”semi-coherent” denotes all interfaces, 1D and 2D, where dislocation cores are still well separated, which is the case for a misfit below about 20%. For convenience and to avoid confusion we use the terms ”small incoherent” and ”large incoherent” supercells/interfaces instead.

We start with the NW Cu/W interface. It is created from the coherent interface by inserting one extra Cu unit cell every 4 unit cells along the x axis and uniformly compressing the Cu slab while uniformly expanding the W slab. Due to the high stress present in the coherent interface, this process releases the compressive stress in the W layer and the tensile stress in the Cu layer. The insertion of the cell introduces a system of dislocations with dislocation lines parallel to the y direc-

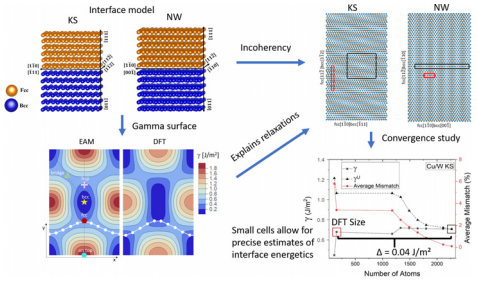

tions spaced at $d = n_{Cu(x,y)} l_{Cu(x,y)} + \delta_{SB}$ along x, which corresponds to about 12.7 Å. Here, δ_{SB} denotes the small correction introduced by the stress-balancing approach. The Burgers vector corresponds to 1/2[110]

or [001] when referring to the fcc and bcc lattice, respectively. In contrast to the coherent interface, where atoms in the interface are in the minimum of the gamma surface everywhere, the large incoherent interface samples the gamma surface on a line connecting two neighboring minima. An example minimum is marked by the green circle in Fig. 5. The exact path in the gamma surface plot taken between the minima depends on the geometric positions of the atoms.

For the initial structure, which was uniformly stretched and compressed with respect to the coherent case, the local relative displacement vector $\boldsymbol{u}$ (i.e. position in the gamma surface plot) is linear in x with $\boldsymbol{u} = (w * x, 0)$, where w is given by $w = b/d$ and b is the magnitude of the Burgers vector. In the gamma surface (Fig. 4), the path runs from the bottom left corner to the bottom right corner, i.e. from the minimum over the maximum again to the minimum in straight fashion in the x direction. As seen in Fig. 5b, the unrelaxed structure exhibits the dislocation core where Cu and Me are aligned on top of each other (red circle) as this corresponds to the maximum of the gamma surface. The regions where Cu and Me are displaced (green circle) are in the minimum of the gamma surface and correspond to the non-dislocated coherent interface.

Figure 5 also shows the relaxed structures according to DFT and EAM. Relaxation changes the geometric structure and the path in the gamma surface quite significantly compared to the unrelaxed interface. Both DFT and EAM show the same relaxation pattern, which points to the validity of the EAM potential for structure relaxation. For a given Cu atom situated at position $\boldsymbol{r}_i$, the displacement $\boldsymbol{u}(\boldsymbol{r}_i)$ is calculated as the difference in the position projected onto the $x - y$ plane with respect to the position of the neighboring W atom, also projected onto the same plane. The corresponding path $\boldsymbol{u}(\boldsymbol{r}_i)$ is shown also in Fig. 4 with white points. As a main feature, the Cu slab shifts rigidly relative to the W slab so that the interface avoids both maximum and minimum and moves on an intermediate portion of the gamma surface throughout. In other words, instead of moving from the bcc site over the on top site back to the bcc site, the path moves from the hcp site over bridge to the fcc site, although these sites are higher in energy (0.63 J/m^2) compared to the bcc site (0 J/m^2) but much lower than the energy corresponding to the top site (1.92 J/m^2). Indeed, in the relaxed geometry the site-averaged γ (calculated as suggested in [29]) is 0.36 J/m^2 while for the start geometry it is 0.47 J/m^2. While we do not aim for a quantitative modeling of interface energetics based on the gamma surface here, the calculation of the average γ elucidates the reason for the general rigid shift.

This general shift of the path for the NW interface has not been discussed before in any work on misfit dislocations. This is probably due to the fact that either investigations on NW interfaces did not particularly focus on the gamma surface or the works were not dealing with $bcc - fcc$ interfaces but rather with other ones with different gamma surface topology. Note that the procedure described in [14] to identify dislocation cores based on the relaxation pattern is not applicable to the present small incoherent interface because of this rigid shift. In general, the shift can be expected to occur if the dislocations are narrowly spaced and therefore it depends on the mismatch between fcc and bcc lattices whether the particular structure shown in Fig. 5 will appear in experiments.

The KS interfaces show a quite different interface structure, as illustrated in Fig. 5. The unrelaxed structure would include regions where Cu and Me are on top (maximum) or displaced by half period (minimum) as marked again by circles. The relaxation again reveals the trend to avoid the on top regions. A large portion of the interface adopts the bcc stacking while smaller areas are also in fcc, hcp or bridge stacking. The interface geometry is essentially the same in DFT simulations for Nb and W. Some differences arise between Nb and W in EAM simulations, but they are not pronounced.

For completeness, small incoherent supercells along the y direction were also investigated for the NW orientation where dislocations are created with 1/2[112] Burgers vector. As expected, the relaxation dissociates the dislocations into two 1/2[101] and 1/2[011] Burgers vector due to Frank's rule. The representation of this dissociation is shown for Cu/Nb in the Appendix (Fig. 11).

3.2.3. Large incoherent interfaces cells

Figure 6 shows the largest cells treated with EAM which correspond to the black rectangles in Fig. 2. These larger cells have dislocations in both x and y direction, hence the resulting interface geometry is more complex. For both the NW and KS interfaces, the maximum of the gamma surface is now also appearing at specific points in the interface since the whole area of the gamma surface is sampled and the maximum cannot be totally avoided like for smaller cells. Interestingly, while these cells are larger and structurally more complex, the relaxation changes the interface structure only little. Essentially one can recognize that the on top region shrinks somewhat by the relaxation. Neither the rigid shift nor the dissociation, which were responsible for the considerable difference between relaxed and unrelaxed structures of the small incoherent NW supercells, are observed here.

In terms of dislocation network, previous investigations have rationalized the relaxed geometry based on linear elasticity [59] or with an atomically informed Frank-Bilby theory [14]. Such investigations are not attempted here. However, we note that, if a dislocation with a dislocation line along y and with the Burgers vector 1/2[−110] intersects a dislocation along x with the Burgers vector 1/2[112], at the intersection the displacement is equal to 1/2[011]. This corresponds to the minimum of the gamma surface. Therefore, in contrast to other interface topologies, where the dislocation intersection is an energetic maximum [34], in the present case the intersection results in an energetic minimum. It is clear that in this case the analysis proposed in [14], where dislocation cores are identified based on maximum displacements of the atoms, is not suitable since in the intersection point no relaxation will occur. Therefore, we prefer to interpret the obtained geometry of the interface mainly in terms of the gamma surface, which clearly guides the relaxations in all cases.

To summarize, the geometry at the interface changes for different sizes of the unit cell. The structure of the large incoherent supercells can be expected to give a good representation of what should be observed in experiment of NW and KS interfaces. The question remains how much the different interfaces with their different misfit dislocation networks differ in energy. In general, γ as defined by Eq. (5) can be expected to correlate with the site-averaged gamma surface. However, also elastic distortions contribute to γ and, therefore, the exact variation is best evaluated explicitly with EAM to understand how strongly different interface structures affect γ. This is the topic of the next section.

3.3. Cell size convergence

One of the main aims of this paper is to evaluate whether the small cell sizes used for DFT calculations are appropriate. As DFT convergence studies require a significant amount of computational resources, the EAM is utilised to investigate cell size effects on γ and WoS.

Figure 7 illustrates how the γ values and γ^U change as the number of atoms increases for the KS interface. In order to achieve convergence, cells with different numbers of atoms and different mismatches along x and y have been examined. For this convergence test we use also the semi-convergent terms of the continued fractions which minimize $M_{(x,y)}$ instead of $\Delta_{(x,y)}$. An in-detail list of all the computed γ values and WoS for increasing cell sizes can be found in the Appendix (Table 2 and Table 3).

Figure 7 shows that in general both γ and γ^U converge with larger cell size. As expected, γ converges much faster than γ^U since it does not contain the elastic distortion in the slabs. For γ^U, the interface energy drops with increasing cell size since elastic strain is released gradually in the cells. For Cu/W, γ^U can only be considered to be converged at about 2000 atoms. For Cu/Nb, the convergence is faster, which we attribute to the fact that Nb is elastically softer compared to W. For γ, the

convergence is achieved at much smaller cell sizes of about 200 atoms. γ slightly increases with increasing cell size since the interface samples the gamma surface more completely with increasing cell size (see previous section) and must also include the energetically more unfavorable regions. In general, the γ values converge to around 0.71 J/m^2 for the Cu/W case and to around 0.54 J/m^2 for Cu/Nb.

The convergence of the NW interface can be assumed to follow the general trend observed for KS. Values for γ are shown in the Appendix (Table 2, Table 3), where it can be seen that for 200 atoms γ converges reasonably well. In general, the NW orientation has lower γ values compared to KS. For Cu/W, converged values are 0.64 J/m^2 while for Cu/Nb the values are 0.42 J/m^2. We conclude from the convergence testing that the small interface cells already provide reliable γ values.

3.4. EAM/DFT comparison

Finally, we explore the energy differences between DFT and EAM calculations. Since the error of γ due to the small cell size is minor, DFT provides a benchmark for the values of γ and WoS. For a better understanding we also include γ_S in the subsequent comparison.

3.4.1. Surface energies

γ_S of the pure Cu, Nb and W metals were computed for four different orientations, corresponding to the most commonly reported interface relations between *fcc* and *bcc* metals. As can be seen in Fig. 8, γ_S for Cu corresponding to the (111), (112) and (110) planes follow the same trend for both DFT and EAM, but the absolute values are shifted. A stronger shift of about 0.5 J/m^2 compared to DFT is observed for the EAM potential of Zhou et al. [50] while the energies obtained using the potential by Demkowicz et al. [10] are shifted by about 0.25 J/m^2. For the W surfaces, EAM reveals the smallest surface energy for the (110) orientation, in agreement with DFT. The other two orientations have a comparable γ_S for EAM while DFT predicts a higher energy for the (100) orientation. A similar observation has been made previously in ref. [56] where DFT was compared to a MEAM potential. For Nb, the EAM potential accurately matches the DFT surface energies for all 3 examined surfaces (see Fig. 8). Generally speaking, the EAM potential for Cu/W shows a stronger disagreement with DFT compared to the Cu/Nb potential, which we attribute to the fact that the Cu/W forcefield was not fitted specifically to surfaces and interfaces [50].

3.4.2. Interface energies and work of separation

Figure 9 shows the comparison of γ and WoS between EAM and DFT. For Cu/W in both NW and KS orientations, DFT shows significantly higher values for γ compared to EAM. More specifically, DFT γ values are 0.53 J/m^2 and 0.64 J/m^2 higher than the corresponding EAM values for the NW and KS interfaces. For Cu/Nb, the DFT values are 0.21 J/m^2 and 0.22 J/m^2 lower compared to EAM for NW and KS, respectively. Comparing the γ values obtained with EAM to the literature [25,26] where the same potential was used, only a slight deviation can be seen for Cu/Nb, which we attribute to the different cell sizes and methodology. The EAM Cu/W potential shows larger deviations to literature values both when comparing to other EAM calculations [58] and DFT results [27,28]. Noticeably, the DFT result from Ref. [27] closely matches our DFT result while the DFT result from Wang et al. [28] differs significantly. We attribute this discrepancy to the use of different lateral dimensions of the cell used for the calculation of the coherent cells in [27,28].

Importantly our investigation clearly reveals that calculating γ with small incoherent supercells using DFT gives a much more precise prediction for γ compared to using large incoherent supercells with EAM. As a general feature, DFT predicts γ values to be about twice as high for Cu/W compared to Cu/Nb. In addition, the NW interface is energetically slightly favorable over the KS orientation. EAM also reproduces the latter observation consistently but fails to reproduce the trend between Cu/W and Cu/Nb.

The WoS values for Cu/W obtained using the potential developed by Zhou et al. [50] were found to closely match the respective DFT values, with a difference of only 0.04 J/m^2 (NW) and 0.14 J/m^2 (KS), respectively. The calculated WoS for Cu/Nb using the potential developed by Demkowicz and Hoagland [10] on the other hand shows a considerable offset to the DFT calculations of 0.57 J/m^2 (NW) and 0.61 J/m^2 (KS), respectively. Therefore, although the potential developed by Demkowicz and Hoagland [10] was found to describe more accurately the γ values and the surface energies of the pure metallic *fcc* and *bcc* systems compared to the potential developed by Zhou et al. [50], this is not reflected in more accurate values for the WoS.

4. Conclusions

We have studied the structure and energetic properties of Cu/Nb and Cu/W interfaces. Two different interface orientations, i.e. the KS and NW orientation, have been examined using DFT and EAM. To explore the structural differences, three different types of interface supercells were investigated, i.e. the coherent, the small incoherent and the large incoherent supercell. For the coherent supercell, the gamma surface was evaluated and the general topology was found to compare well between DFT and EAM. As a consequence, the atomistic structure of the small incoherent interfaces was found to be in close agreement between EAM and DFT. The NW interface exhibits a rigid shift of the Cu slab with respect to the W slab, which can be expected to be observed in experiment for Cu/W where already the small incoherent supercell has negligible mismatch. The KS interfaces exhibit less ordered structures, which correlate with their generally higher interface energies compared to the NW interfaces. The large incoherent interfaces, which could be treated only with EAM due to their considerable cell size, exhibit a more complex structure and sample the gamma surface more comprehensively. As a result, the energies of these interfaces are slightly higher compared to the small incoherent cells. The main feature of the structural relaxation of the interface is the avoidance of the maximum of the gamma surface.

The energetic changes between small and large incoherent interfaces are not pronounced, which shows that former already provide reliable values. Indeed, the deviations are 0.003 J/m^2 and 0.03 J/m^2 for the NW and KS orientation, respectively. For Cu/Nb, the corresponding deviations are 0.04 J/m^2 and 0.03 J/m^2. Thus, the results show that accurate results can be achieved using cell sizes with less than 250 atoms which are accessible to DFT simulations.

Regarding the two examined EAM potentials, the obtained geometric structures were shown to match the DFT calculations well. The interface energies are closer to the DFT results for Cu/Nb with the force field of Demkowicz et al. [10]. The potential of Zhou et al. [50] was found to considerably underestimate interface energies for Cu/W. We attribute this disagreement to deviations in surface energy which were analysed in detail previously [56].

In conclusion, our results provide reliable DFT values for interface energies and WoS for the Cu/Nb and Cu/W system. They improve the theoretical understanding of such interfaces and can be used as an input in future thermodynamic and mechanical modeling to describe precipitation, segregation, crack propagation or delamination phenomena.

Declaration of Competing Interest

The authors declare that they have no known competing financial interests or personal relationships that could have appeared to influence the work reported in this paper.

Acknowledgements

The authors would like to acknowledge Infineon Technologies, Austria for financial support. A.L.S. acknowledges funding by EPSRC (grant EP/P013503/1). V.F. would like to acknowledge funding by EPSRC (grant EP/L015862/1) as part of the CDT in molecular

Table 2
EAM Interface energies comparison for Cu/W.

Orientation/Number of Atoms	γ (J/m^2)	$n_{Cu(x)}/n_{Me(x)}, n_{Cu(y)}/n_{Me(y)}$	Mismatch x(%)/y(%)
KS/114	0.448	1/1,5/3	6.8/4.8
KS/156	0.678	1/1,7/4	6.7/0.1
KS/1176	0.660	8/7,7/4	6.6/0.1
KS/1332	0.719	9/8,7/4	4.9/0.1
KS/1488	0.717	10/9,7/4	3.6/0.1
KS/1644	0.714	11/10,7/4	2.6/0.1
KS/1800	0.712	12/11,7/4	1.6/0.1
KS/2112	0.709	13/14,7/4	0.4/0.1
KS/2268	0.7108	15/14,7/4	0.1/0.1
NW/84	0.637	4/3,1/1	3.8/1.4
NW/108	0.635	5/4,1/1	0.7/1.4
NW/564	0.632	21/26,1/1	0.0/1.4

Table 3
EAM Interface energies comparison for Cu/Nb.

Orientation/Number of Atoms	γ (J/m^2)	$n_{Cu(x)}/n_{Me(x)}, n_{Cu(y)}/n_{Me(y)}$	Mismatch x(%)/y(%)
KS/42	0.486	1/1,2/1	10.6/45.2
KS/156	0.512	1/1,7/4	10.6/4.2
KS/198	0.514	1/1,9/5	10.6/1.4
KS/240	0.511	1/1,11/6	10.6/0.4
KS/1332	0.557	6/5,11/6	7.3/0.4
KS/1572	0.553	7/6,11/6	4.3/0.4
KS/1812	0.547	8/7,11/6	2.2/0.4
KS/2052	0.542	9/8,11/6	0.6/0.4
KS/2292	0.540	10/9,11/6	0.6/0.4
KS/4344	0.542	19/17,11/6	0.0/0.4
NW/84	0.475	4/3,1/1	3.3/5.2
NW/192	0.454	9/7,1/1	0.1/5.2
NW/3564	0.491	9/7,19/18	0.1/0.4

Table 4
WoS and interface energies comparison between EAM and DFT.

Interface	γ EAM (J/m^2)	γDFT (J/m^2)	WoS EAM (J/m^2)	WoS DFT (J/m^2)	Number of Atoms
Cu/W NW	0.64	1.17	3.44	3.4	108
Cu/W KS	0.68	1.32	3.36	3.22	114
Cu/W KS	0.71	-	3.36	-	2268
Cu/Nb NW	0.49	-	2.4	-	3564
Cu/Nb KS	0.54	-	2.38	-	2052
Cu/Nb NW	0.45	0.24	2.5	3.07	192
Cu/Nb KS	0.51	0.29	2.45	3.06	240

Table 5
Elastic constants used for the stress-balancing method.

Element	C_{11} (GPa)	C_{12} (GPa)	C_{44} (GPa)
Cu	167	121	70
W	516	198	143
Nb	233	145	11

modeling and materials science. Computational resources on Archer (http://www.archer.ac.uk) were provided via our membership of the UK's HPC Materials Chemistry Consortium, which is funded by EPSRC (EP/L000202, EP/R029431). R.B., J.S. and L.R. gratefully acknowledge the financial support under the scope of the COMET program within the K2 Center "Integrated Computational Material, Process and Product Engineering (IC-MPPE)" (Project No. 859480). This program was supported by the Austrian Federal Ministries for Climate Action, Environment, Energy, Mobility, Innovation and Technology (BMK) and for Digital and Economic Affairs (BMDW), represented by the Austrian research funding association (FFG), and the federal states of Styria, Upper Austria, and Tyrol. V.F. and A.L.S. would like to thank Jack Strand, Tom Durrant and David Schmidt for useful comments and help in calculations. The computational results presented have been achieved in part using the Vienna Scientific Cluster (VSC). L.R. would like to acknowledge funding by the Austrian Science Fund (FWF) [P 34179-N].

Tables 2, 3, 4 and 11.

References

[1] I.J. Beyerlein, N.A. Mara, J. Wang, J.S. Carpenter, S.J. Zheng, W.Z. Han, R.F. Zhang, K. Kang, T. Nizolek, T.M. Pollock, Structure–property–functionality of bimetal interfaces, Jom 64 (10) (2012) 1192–1207.
[2] Y. Gao, T. Yang, J. Xue, S. Yan, S. Zhou, Y. Wang, D.T. Kwok, P.K. Chu, Y. Zhang, Radiation tolerance of Cu/W multilayered nanocomposites, J. Nucl. Mater. 413 (1) (2011) 11–15.
[3] G.C. Ma, J.L. Fan, H.R. Gong, Fundamental effects of hydrogen on cohesion properties of Cu/W interfaces, Solid State Commun. 250 (July 2016) (2017) 79–83.
[4] S. Zheng, I.J. Beyerlein, J.S. Carpenter, K. Kang, J. Wang, W. Han, N.A. Mara, High-strength and thermally stable bulk nanolayered composites due to twin-induced interfaces, Nat. Commun. 4 (1) (2013) 1696, doi:10.1038/ncomms2651.
[5] M.M. Primorac, M.D. Abad, P. Hosemann, M. Kreuzeder, V. Maier, D. Kiener, Elevated temperature mechanical properties of novel ultra-fine grained Cu-Nb composites, Mater. Sci. Eng., A 625 (2015) 296–302.
[6] B. Girault, D. Eyidi, T. Chauveau, D. Babonneau, P.-O. Renault, E. Le Bourhis, P. Goudeau, Copper coverage effect on tungsten crystallites texture development in W/Cu nanocomposite thin films, J. Appl. Phys. 109 (1) (2011) 014305.
[7] Z. Liu, M. Monclús, L. Yang, M. Castillo-Rodríguez, J. Molina-Aldareguía, J. LLorca, Tensile deformation and fracture mechanisms of Cu/Nb nanolaminates studied by in situ TEM mechanical tests, Extreme Mech. Lett. 25 (2018) 60–65.
[8] L. Zhu, X. Zheng, Influence of interface energy and grain boundary on the elastic modulus of nanocrystalline materials, Acta Mech. 213 (3–4) (2010) 223–234.

[9] Y. Zhu, The interface energy and particle size effects on nanocomposites, UCLA Electronic Theses and Dissertations, 2019 Ph.D. thesis.
[10] M. Demkowicz, R. Hoagland, Structure of Kurdjumov–Sachs interfaces in simulations of a copper–niobium bilayer, J. Nucl. Mater. 372 (1) (2008) 45–52.
[11] S. Zheng, J.S. Carpenter, R.J. McCabe, I.J. Beyerlein, N.A. Mara, Engineering interface structures and thermal stabilities via SPD processing in bulk nanostructured metals, Sci. Rep. 4 (2014) 4226.
[12] G. Kurdjumov, G. Sachs, Over the mechanisms of steel hardening, Z. Phys. 64 (1930) 325–343.
[13] Z. Nishiyama, X-ray investigation of the mechanism of the transformation from face centered cubic lattice to body centered cubic, Sci. Rep. Tohoku Univ. 23 (1934) 637.
[14] J. Wang, R.F. Zhang, C.Z. Zhou, I.J. Beyerlein, A. Misra, Interface dislocation patterns and dislocation nucleation in face-centered-cubic and body-centered-cubic bicrystal interfaces, Int. J. Plast. 53 (2014) 40–55.
[15] M. Monclús, M. Karlik, M. Callisti, E. Frutos, J. LLorca, T. Polcar, J. Molina-Aldareguía, Microstructure and mechanical properties of physical vapor deposited Cu/W nanoscale multilayers: influence of layer thickness and temperature, Thin Solid Films 571 (2014) 275–282.
[16] L. Zhang, E. Martinez, A. Caro, X.-Y. Liu, M.J. Demkowicz, Liquid-phase thermodynamics and structures in the Cu-Nb binary system, Modell. Simul. Mater. Sci. Eng. 21 (2) (2013) 025005, doi:10.1088/0965-0393/21/2/025005.
[17] R. Banerjee, A. Puthucode, S. Bose, P. Ayyub, Nanoscale phase separation in amorphous immiscible copper-niobium alloy thin films, Appl. Phys. Lett. 90 (2) (2007) 021904.
[18] W.P. Davey, The lattice parameter and density of pure tungsten, Phys. Rev. 26 (6) (1925) 736.
[19] C. Hou, X. Song, F. Tang, Y. Li, L. Cao, J. Wang, Z. Nie, W–Cu composites with submicron-and nanostructures: progress and challenges, NPG Asia Mater. 11 (1) (2019) 1–20.
[20] R.L. Barns, Niobium: lattice parameter and density, J. Appl. Phys. 39 (8) (1968) 4044–4045, doi:10.1063/1.1656912.
[21] M. Straumanis, L. Yu, Lattice parameters, densities, expansion coefficients and perfection of structure of Cu and of Cu–in α phase, Acta Cryst. 25 (6) (1969) 676–682.
[22] S. Plimpton, Fast parallel algorithms for short-range molecular dynamics, J. Comput. Phys. 117 (1) (1995) 1–19.
[23] R. Zhang, J. Wang, I. Beyerlein, T. Germann, Dislocation nucleation mechanisms from fcc/bcc incoherent interfaces, Scr. Mater. 65 (11) (2011) 1022–1025.
[24] J. Wang, R. Zhang, C. Zhou, I.J. Beyerlein, A. Misra, Characterizing interface dislocations by atomically informed frank-bilby theory, J. Mater. Res 28 (13) (2013) 1646–1657.
[25] M.J. Demkowicz, L. Thilly, Structure, shear resistance and interaction with point defects of interfaces in Cu-Nb nanocomposites synthesized by severe plastic deformation, Acta Mater. 59 (20) (2011) 7744–7756.
[26] J. Zhou, R.S. Averback, P. Bellon, Stability and amorphization of Cu-Nb interfaces during severe plastic deformation: molecular dynamics simulations of simple shear sciencedirect stability and amorphization of cu - Nb interfaces during severe plastic deformation : molecular dynamics simulations of simple shear, Acta Mater. 73 (July) (2014) 116–127.
[27] C.P. Liang, J.L. Fan, H.R. Gong, X. Liao, X. Zhu, S. Peng, Interface structure and work function of W-Cu interfaces, Appl. Phys. Lett. 103 (21) (2013).
[28] J.W. Wang, J.L. Fan, H.R. Gong, Effects of Zr alloying on cohesion properties of Cu/W interfaces, J. Alloys Compd. 661 (2016) 553–556.
[29] S. Lu, Q.M. Hu, M.P. Punkkinen, B. Johansson, L. Vitos, First-principles study of fcc-Ag/bcc-Fe interfaces, Phys. Rev. B 87 (22) (2013) 1–11, doi:10.1103/PhysRevB.87.224104.
[30] B. Shan, L. Wang, S. Yang, J. Hyun, N. Kapur, Y. Zhao, J.B. Nicholas, K. Cho, First-principles-based embedded atom method for PdAu nanoparticles, Phys. Rev. B 80 (3) (2009) 035404.
[31] W.-S. Ko, D.-H. Kim, Y.-J. Kwon, M.H. Lee, Atomistic simulations of pure tin based on a new modified embedded-atom method interatomic potential, Metals 8 (11) (2018) 900.
[32] E. Symianakis, A. Kucernak, Embedded atom method interatomic potentials fitted upon density functional theory calculations for the simulation of binary PtNi nanoparticles, Comput. Mater. Sci 133 (2017) 185–193.
[33] S.A.E. Johansson, M. Christensen, G. Wahnström, Interface energy of semicoherent metal-Ceramic interfaces, Phys. Rev. Lett. 95 (22) (2005) 226108.
[34] S. Lu, J. Ågren, L. Vitos, Ab initio study of energetics and structures of heterophase interfaces: from coherent to semicoherent interfaces, Acta Mater. 156 (2018) 20–30, doi:10.1016/j.actamat.2018.06.030.
[35] Y. Linghu, X. Wu, R. Wang, W. Li, Q. Liu, The adhesive properties of coherent and semicoherent NiAl/V interfaces within the Peierls-Nabarro model, Crystals 6 (4) (2016) 1–16, doi:10.3390/cryst6040032.
[36] Y. Zhang, Y. Yao, The two-dimensional Peierls-Nabarro model for interfacial misfit dislocation networks of cubic lattice, Eur. Phys. J. B 55 (4) (2007) 355–362, doi:10.1140/epjb/e2007-00072-0.
[37] Y. Zhang, Y. Yao, The multiscale model combining elastic theory with AB initio calculations for metal-ceramic interfaces, Mod. Phys. Lett. B 22 (32) (2008) 3135–3143, doi:10.1142/S0217984908017667.
[38] N. Medvedeva, Y. Gornostyrev, O. Kontsevoi, A. Freeman, Ab-initio study of interfacial strength and misfit dislocations in eutectic composites: NiAl/Mo, Acta Mater. 52 (3) (2004) 675–682, doi:10.1016/j.actamat.2003.10.004.
[39] Y. Yao, T. Wang, The modified Peierls-Nabarro model of interfacial misfit dislocation, Acta Mater. 47 (10) (1999) 3063–3068, doi:10.1016/S1359-6454(99)00147-0.
[40] Y. Yao, T. Wang, C. Wang, Peierls-Nabarro model of interfacial misfit dislocation: an analytic solution, Phys. Rev. B 59 (1999) 8232–8236, doi:10.1103/PhysRevB.59.8232.
[41] G. Kresse, J. Hafner, Ab initio molecular dynamics for liquid metals, Phys. Rev. B 47 (1) (1993) 558–561, doi:10.1103/PhysRevB.47.558.
[42] G. Kresse, J. Hafner, Ab initio molecular-dynamics simulation of the liquid-metal–amorphous-semiconductor transition in germanium, Phys. Rev. B 49 (20) (1994) 14251–14269, doi:10.1103/PhysRevB.49.14251.
[43] J.P. Perdew, J.A. Chevary, S.H. Vosko, K.A. Jackson, M.R. Pederson, D.J. Singh, C. Fiolhais, Atoms, molecules, solids, and surfaces: applications of the generalized gradient approximation for exchange and correlation, Phys. Rev. B 46 (11) (1992) 6671.
[44] J.P. Perdew, K. Burke, M. Ernzerhof, Generalized gradient approximation made simple, Phys. Rev. Lett. 77 (18) (1996) 3865–3868, doi:10.1103/PhysRevLett.77.3865.
[45] S. Jana, K. Sharma, P. Samal, Assessing the performance of the recent meta-GGA density functionals for describing the lattice constants, bulk moduli, and cohesive energies of alkali, alkaline-earth, and transition metals, J. Chem. Phys. 149 (16) (2018) 164703.
[46] A. Patra, J.E. Bates, J. Sun, J.P. Perdew, Properties of real metallic surfaces: effects of density functional semilocality and van der Waals nonlocality, Proc. Natl. Acad. Sci. 114 (44) (2017) E9188–E9196.
[47] J. Inglesfield, Adhesion between al slabs and mechanical properties, J. Phys. F 6 (5) (1976) 687.
[48] A.H. Larsen, J.J. Mortensen, J. Blomqvist, I.E. Castelli, R. Christensen, M. Dułak, J. Friis, M.N. Groves, B. Hammer, C. Hargus, et al., The atomic simulation environment–a python library for working with atoms, J. Phys. 29 (27) (2017) 273002.
[49] R. Fletcher, Practical Methods of Optimization, John Wiley & Sons, 2013.
[50] X. Zhou, R. Johnson, H. Wadley, Misfit-energy-increasing dislocations in vapor-deposited CoFe/NiFe multilayers, Phys. Rev. B 69 (14) (2004) 144113.
[51] E.B. Tadmor, R.S. Elliott, J.P. Sethna, R.E. Miller, C.A. Becker, The potential of atomistic simulations and the knowledgebase of interatomic models, Jom 63 (7) (2011) 17.
[52] C.A. Becker, F. Tavazza, Z.T. Trautt, R.A.B. de Macedo, Considerations for choosing and using force fields and interatomic potentials in materials science and engineering, Curr. Opin. Solid State Mater. Sci. 17 (6) (2013) 277–283.
[53] F. Barthelat, R. Rabiei, Toughness amplification in natural composites, J. Mech. Phys. Solids 59 (4) (2011) 829–840.
[54] K. Momma, F. Izumi, Vesta: a three-dimensional visualization system for electronic and structural analysis, J. Appl. Crystallogr. 41 (3) (2008) 653–658.
[55] M.N. Popov, J. Spitaler, M. Mühlbacher, C. Walter, J. Keckes, C. Mitterer, C. Draxl, TiO2(100)/Al2O3(0001) interface: a first-principles study supported by experiment, Phys. Rev. B 86 (20) (2012) 205309.
[56] D. Scheiber, R. Pippan, P. Puschnig, L. Romaner, Ab initio calculations of grain boundaries in bcc metals, Modell. Simul. Mater. Sci. Eng. 24 (3) (2016) 035013.
[57] A. Hashibon, C. Elsässer, Y. Mishin, P. Gumbsch, First-principles study of thermodynamical and mechanical stabilities of thin copper film on tantalum, Phys. Rev. B 76 (2007) 245434, doi:10.1103/PhysRevB.76.245434.
[58] A. Ruffini, J. Durinck, J. Colin, C. Coupeau, J. Grilhé, Gliding at interface during thin film buckling: acoupled atomistic/elastic approach, Acta Mater. 60 (3) (2012) 1259–1267, doi:10.1016/j.actamat.2011.11.041.
[59] A. Vattré, N. Abdolrahim, S.S. Navale, M.J. Demkowicz, The relaxed structure of intrinsic dislocation networks in semicoherent interfaces: predictions from anisotropic elasticity theory and comparison with atomistic simulations, Extreme Mech. Lett. 28 (2019) 50–57, doi:10.1016/j.eml.2019.02.003.